Data report: compressional wave velocity measurements on sediments from the reference site off Kumano, Nankai Trough, NantroSEIZE Expedition 333[1]

Yoshitaka Hashimoto[2] and Mika Yamaguchi[2]

Chapter contents

[1] Hashimoto, Y., and Yamaguchi, M., 2014. Data report: compressional wave velocity measurements on sediments from the reference site off Kumano, Nankai Trough, NantroSEIZE Expedition 333. *In* Henry, P., Kanamatsu, T., Moe, K., and the Expedition 333 Scientists, *Proc. IODP,* 333: Tokyo (Integrated Ocean Drilling Program Management International, Inc.). doi:10.2204/iodp.proc.333.202.2014
[2] Department of Applied Science, Kochi University, Akebonocyo 2-5-1, Kochi 780-8520, Japan. Correspondence author: **hassy@kochi-u-ac.jp**

Abstract

Compressional wave velocities were measured for sediments from the reference site for the Nankai subduction zone, obtained during Integrated Ocean Drilling Program Nankai Trough Seismogenic Experiment (NanTroSEIZE) Expedition 333. The samples were cored at Sites C0011 and C0012. Five samples were tested from each site. Laboratory tests were conducted with controlled pore fluid pressure and confining pressure. We also measured porosity change during experiments using the change in fluid volume.

Porosity measured on board ranges from ~0.50 to ~0.69 for Site C0011 from ~70 to ~380 meters below seafloor (mbsf) and from ~0.49 to ~0.70 for Site C0012 from ~60 to ~165 mbsf.

Compressional wave velocity ranges from ~1510 to 1770 m/s at Site C0011 and ~1510 to 1680 m/s at Site C0012, under hydrostatic fluid pressure conditions at the sampling depth.

Introduction

The change in physical properties from incoming sediment to accretionary prisms is a key to understanding mass balance of sediments, fluid flux, heat transportation, wedge architecture, and seismic behavior at a subduction interface (e.g., Bangs and Westbrook, 1991; von Huene and Scholl, 1991; Moore and Vrolijk, 1992; Erickson and Jarrard, 1998; Bilek and Lay, 1999; Moore and Saffer, 2001; Gettemy and Tobin, 2003; Saffer, 2007). Although Integrated Ocean Drilling Program (IODP) Nankai Trough Seismogenic Experiment (NanTroSEIZE) Stage 1 was conducted targeting sediments in the wedge, slope basins, backarc basin, decollement, and shallow portion of the megasplay fault, incoming sediments at the reference sites located oceanward of the deformation front were drilled during IODP NanTroSEIZE Stage 2 Expeditions 322 and 333. Incoming sediments at the reference sites represent the state before subduction and in this respect are very important to understanding the change in physical properties after underthrusting. In addition, because the sediments at the reference sites are considered to be in a normal compaction state, the porosity-velocity relationship can be used to convert velocity into porosity and also into pore pressure (e.g., Saffer, 2007).

We measured compressional wave velocity at a variety of effective pressures to examine the relationship between porosity and veloc-

doi:10.2204/iodp.proc.333.202.2014

ity for sediments from Sites C0011 and C0012 from Expedition 333.

Site locations and lithologies

Site C0011

Site C0011 is located at the northern flank of the Kashinosaki Knoll (Figs. F1, F2). A total of 380 m of cores was obtained from Holes C0011C and C0011D (Fig. F3). Lithology is divided into two units (Units I and II) at 347.82 m core depth below seafloor, method B (CSF-B) (see the "Site C0011" chapter [Expedition 333 Scientists, 2012a]), corresponding to Shikoku Basin hemipelagites and middle Shikoku Basin volcanic sand faces, respectively (see the "Expedition 333 summary" chapter [Underwood et al., 2010]). Unit I is divided into Subunits 1A and 1B at 251.56 m CSF-B. Subunit IA is mainly composed of greenish gray silty clay with minor amounts of volcanic ash. Subunit IB comprises weakly lithified mudstone with minor altered volcanic glass and volcanic ash. The dominant lithology of Unit II is coarser grained tuffaceous sandstones and conglomerate interbedded with mudstone similar to that of Subunit IB. The dip angle of bedding is stably low, at ~10°. Moderately dipping small faults and planar shear zones are distributed in the 30–190 m CSF-B interval. Porosity determined onboard is about 0.63 in the ~20–80 m CSF-B interval and slightly increases to ~0.68 at ~80 m CSF-B. Again, porosity of 0.69 is constant to ~250 m CSF-B. Deeper than 250 m CSF-B, porosity decreases to 0.55 immediately and slightly decreases to ~0.5 to 380 m CSF-B.

Five core samples from Site C0011 were tested for velocity measurements. The locations of samples for this site are shown in Table T1 and Figure F3. Tested samples are from Sections 333-C0011D-6H-3, 14H-3, 31X-5, 40X-2, and 50X-3. All samples are silty clay or weakly lithified mudstone. Dip angles of bedding for those samples are 13°, 16°, 19°, 19°, and 10°, respectively. Those values are determined from structure data at the location closest to the analyzed samples.

Site C0012

Site C0012 is located close to the top of Kashinosaki Knoll, oceanward of Site C0011 (Figs. F1, F2). A total of 180 m of core was drilled at this site. The lithology of Site C0012 is divided into two units (Unit I Shikoku Basin hemipelagite and Unit II middle Shikoku Basin volcanic sand facies; Fig. F4). Unit I is composed of mainly dark greenish gray clay and silty clay and silt interbedded with volcanic ash and minor thin sand (see the "Site C0012" chapter [Expedition 333 Scientists, 2012b]. The boundary between Units I and II is at 151.61 m CSF-B. Unit II comprises mudstone similar to the lower part of Unit I and turbidite sands and sandstones including pebbles, coarse ash, and lapilli tuff. Lower dipping (~10°) bedding changes to higher dipping (~60°) bedding from the seafloor to 15 m CSF-B. In the interval between 15 and 85 m CSF-B, bedding dip is slightly stable around 50°–60°. Deeper than 85 m CSF-B, bedding dip decreases to about 10°–20°. Deeper than ~150 m CSF-B, bedding dip ranges from 10° to 50° to 180 m CSF-B.

Porosity is roughly constant and about 0.7 in the shallower interval between 0 and 80 m CSF-B. It decreases from 0.7 to ~0.6 from 80 to 100 m CSF-B. Again, porosity is stable at 0.6 to 130 m CSF-B, and then porosity decreases to ~0.5 to 180 m CSF-B. Porosity at Site C0012 is relatively lower at Site C0011 at the same depth (Figs. F3, F4) because porosity at Site C0011 does not change from around 0.6–0.7 to 250 m CSF-B.

Tested samples are Sections 333-C0012C-8H-1, 11H-4, and 15H-5 and Sections 333-C0012D-4H-5 and 9H-3. All samples are silty clay or weakly lithified mudstone. Dip angles of bedding for these samples are 50°, 13°, 14°, 16°, and 16°, respectively, on the basis of structural data.

Methods

The design of the experiment is similar to that employed in other studies of saturated marine sediments (e.g., Tobin et al., 1994; Tobin and Moore, 1997; Gettemy and Tobin, 2003; Hashimoto et al., 2010, 2011; Raimbourg et al., 2011).

Two syringe pumps (Teledyne ISCO 1000D) control pore fluid pressure and confining pressure (Fig. F5). A pore pressure of 1000 kPa was maintained under drained conditions. Velocity measurements were conducted under isotropic confining pressure conditions. Confining (effective) pressure was increased stepwise in the measurements, pressurized in 10 s and held for 24 h for the next step. The pressure interval ranges from 700 to 9460 kPa, which is at least 2.5 times in situ effective pressure at the sampling depth for each sample (Fig. F6). In situ effective pressure at the sampling depth was calculated from the accumulation of the bulk density of sediments and hydrostatic pore fluid pressures at the depth of recovery (Figs. F3, F4; Table T1). A total of 5–6 steps were tested until in situ effective pressure, and an additional 5–7 steps were measured at least 2.5 times when in situ effective pressure was achieved. Lead zirconate titanate (PZT) shear wave transducers (500 kHz) were employed in a source-receiver pair. PZT in a shear orientation generates a weak compressional

mode in addition to its primary shear mode to identify *P*- and *S*-wave arrivals in each test. Because *S*-wave arrival time was often difficult to locate within the coda of the *P*-wave arrival, *S*-wave velocity is not shown in this study. Axial displacements were measured during experiments. The change in porosity is obtained from the change in the volume of pore water. The porosity from onboard measurements was used as the porosity at about 100 kPa of effective pressure because the measurements were obtained under atmospheric pressure and wet conditions. In the case that the experimental condition around 100 kPa was not available, the pore volume at 100 kPa was calculated by linear extrapolation from the closest two points of experimental data. The onboard porosity was taken from averaged values of the porosity measured onboard in the 10 m intervals where the sample was obtained at the middle point of the interval (Figs. **F3, F4**). Error of porosity is defined as the standard deviation of onboard porosity data in the averaged intervals. The error ranges from 0.011 to 0.045 and from 0.013 to 0.028 for analyzed samples from Sites C0011 and C0012, respectively.

Samples were formed into a cylindrical shape, about 3.8 cm in diameter and about 4.5 cm in length. Measurement direction is parallel to the core axis.

Results

Compressional wave velocity as a function of effective pressure is shown in Figure **F6** and Table **T1.** The compressional wave velocities from Sites C0011 and C0012 range from ~1480 to ~1680 m/s and ~1500 to ~1620 m/s, respectively, at low effective pressure up to 460 kPa. The velocities for Site C0011 and C0012 under in situ effective pressure condition vary from ~1510 to ~1770 m/s and ~1510 to ~1680 m/s, respectively. Velocity increases with effective pressure. Samples from deeper portions represent higher compressional wave velocity at in situ effective pressure conditions except for the one from Section 333-C0011D-31X-5, which has higher velocity than the others although the depth is in the middle part of the measured samples. Slopes of curves of velocity as a function of effective pressure are higher for shallower samples than for deeper samples.

Change in porosity during experiments as a function of effective pressure is shown in Figure **F7** and Table **T1,** except for Sample 333-C0012C-11H-4 because the change in pore volume was not obtained for the sample. Porosity of tested samples from Sites C0011 and C0012 ranges from ~0.64 to ~0.50 and ~0.72 to ~0.48, respectively, at lower effective pressure. Porosity under in situ effective pressure for Sites C0011 and C0012 varies from ~0.61 to ~0.47 and ~0.69 to ~0.45, respectively. Porosity decreased with effective pressure increment during our experiments. The slopes of the curves of porosity and effective pressure space are comparable except for Sample 333-C0011D-31X-5 (Fig. **F7**).

The relationship between compressional wave velocity and porosity is represented in Figure **F8.** Two curves shown as "EJ98 high consolidation" and "EJ98 normal consolidation" in indicate the global relationship between compressional wave velocity and porosity (Erickson and Jarrard, 1998). Onboard porosity and compressional wave velocity (*z*-direction) for Holes C0011D and C0012A (drilled during Expedition 322) are also represented in Figure **F8.** The slope angles for each sample in the relationship between compressional wave velocity and porosity almost match the EJ98 normal consolidation curve except for Sample 31X-5. The exception of Sample 31X-5 is probably due to irregular deformation of the sample in the test (rubber jacket was partly stuffed in the edge of sample). Most samples from Sites C0011 and C0012 show slightly slower compressional wave velocity than EJ98 normal consolidation curves and onboard measurements, especially in the lower effective pressure (in porosity higher than ~0.6). The differences between velocities from laboratory experiments and onboard measurements are up to 50 m/s. The velocity in lower porosity is relatively consistent with that from onboard measurements and the EJ98 normal consolidation curve. The comparison of compressional wave velocities with depth between laboratory experiments, onboard measurements, and logging while drilling (LWD) for Site C0012H conducted during Expedition 338 is shown in Figure **F9.** Slightly slower velocities for shallower samples are also observed in the interval shallower than 100 m CSF. The samples deeper than 100 m, however, have relatively well-consistent velocities with those from onboard measurements and LWD.

Acknowledgments

We thank Dr. Hugues Raimbourg and Dr. Pierre Henry for their constructive comments and suggestions, which improved this manuscript very much. This research used samples provided by the Integrated Ocean Drilling Program (IODP). This work was supported by a Grant-in-Aid for Scientific Research (B) (21340129) and a Grant-in-aid for Scientific Research in Innovative Areas (21107002).

References

Bangs, N.L.B., and Westbrook, G.K., 1991. Seismic modeling of the decollement zone at the base of the Barbados

Ridge accretionary complex. *J. Geophys. Res.: Solid Earth,* 96(B3):3853–3866. **doi:10.1029/90JB02138**

Bilek, S.L., and Lay, T., 1999. Rigidity variations with depth along interplate megathrust faults in subduction zones. *Nature,* 400:443–446. **doi:10.1038/22739**

Erickson, S.N., and Jarrard, R.D., 1998. Velocity-porosity relationships for water-saturated siliciclastic sediments. *J. Geophys. Res.: Solid Earth,* 103(B12):30385–30406. **doi:10.1029/98JB02128**

Expedition 333 Scientists, 2012a. Site C0011. *In* Henry, P., Kanamatsu, T., Moe, K., and the Expedition 333 Scientists, *Proc. IODP,* 333: Tokyo (Integrated Ocean Drilling Program Management International, Inc.). **doi:10.2204/iodp.proc.333.104.2012**

Expedition 333 Scientists, 2012b. Site C0012. *In* Henry, P., Kanamatsu, T., Moe, K., and the Expedition 333 Scientists, *Proc. IODP,* 333: Tokyo (Integrated Ocean Drilling Program Management International, Inc.). **doi:10.2204/iodp.proc.333.105.2012**

Gettemy, G.L., and Tobin, H.J., 2003. Tectonic signatures in centimeter-scale velocity-porosity relationships of Costa Rica convergent margin sediments. *J. Geophys. Res.: Solid Earth,* 108(B11):2494. **doi:10.1029/2001JB000738**

Hashimoto, Y., Tobin, H.J., and Knuth, M., 2010. Velocity-porosity relationships for slope apron and accreted sediments in the Nankai Trough Seismogenic Zone Experiment, Integrated Ocean Drilling Program Expedition 315 Site C0001. *Geochem., Geophys., Geosyst.,* 11:Q0AD05. **doi:10.1029/2010GC003217**

Hashimoto, Y., Tobin, H.J., Knuth, M., and Harada, A., 2011. Data report: compressional and shear wave velocity measurements on sediment in the hanging wall and footwall of megasplay fault, NanTroSEIZE Stage 1. *In* Kinoshita, M., Tobin, H., Ashi, J., Kimura, G., Lallemant, S., Screaton, E.J., Curewitz, D., Masago, H., Moe, K.T., and the Expedition 314/315/316 Scientists, *Proc. IODP,* 314/315/316: Washington, DC (Integrated Ocean Drilling Program Management International, Inc.). **doi:10.2204/iodp.proc.314315316.217.2011**

Moore, J.C., and Saffer, D., 2001. Updip limit of the seismogenic zone beneath the accretionary prism of southwest Japan: an effect of diagenetic to low-grade metamorphic processes and increasing effective stress. *Geology,* 29(2):183–186. **doi:10.1130/0091-7613(2001)029<0183:ULOTSZ>2.0.CO;2**

Moore, J.C., and Vrolijk, P., 1992. Fluids in accretionary prisms. *Rev. Geophys.,* 30(2):113–135. **doi:10.1029/92RG00201**

Raimbourg, H., Hamano, Y., Saito, S., Kinoshita, M., and Kopf, A., 2011. Acoustic and mechanical properties of Nankai accretionary prism core samples. *Geochem., Geophys., Geosyst.,* 12:Q0AD10. **doi:10.1029/2010GC003169**

Saffer, D.M., 2007. Pore pressure within underthrust sediment in subduction zones. *In* Dixon T.H., and Moore, J.C. (Eds.), *The Seismogenic Zone of Subduction Thrust Faults:* New York (Columbia Univ. Press), 171–209.

Tobin, H.J., and Moore, J.C., 1997. Variations in ultrasonic velocity and density with pore pressure in the décollement zone, northern Barbados Ridge accretionary prism. *In* Shipley, T.H., Ogawa, Y., Blum, P., and Bahr, J.M. (Eds.), *Proc. ODP, Sci. Results,* 156: College Station, TX (Ocean Drilling Program), 125–135. **doi:10.2973/odp.proc.sr.156.018.1997**

Tobin, H.J., Moore, J.C., and Moore, G.F., 1994. Fluid pressure in the frontal thrust of the Oregon accretionary prism: experimental constraints. *Geology,* 22(11):979–982. **doi:10.1130/0091-7613(1994)022<0979:FPITFT>2.3.CO;2**

Underwood, M.B., Saito, S., Kubo, Y., and the Expedition 322 Scientists, 2010. Expedition 322 summary. *In* Saito, S., Underwood, M.B., Kubo, Y., and the Expedition 322 Scientists, *Proc. IODP,* 322: Tokyo (Integrated Ocean Drilling Program Management International, Inc.). **doi:10.2204/iodp.proc.322.101.2010**

von Huene, R., and Scholl, D.W., 1991. Observations at convergent margins concerning sediment subduction, subduction erosion, and the growth of the continental crust. *Rev. Geophys.,* 29(3):279–316. **doi:10.1029/91RG00969**

Initial receipt: 29 September 2013
Acceptance: 24 August 2014
Publication: 1 October 2014
MS 333-202

Figure F1. Map showing locations of Sites C0011 and C0012 with bathymetry off Kii Peninsula. Map of Japan is shown in upper right.

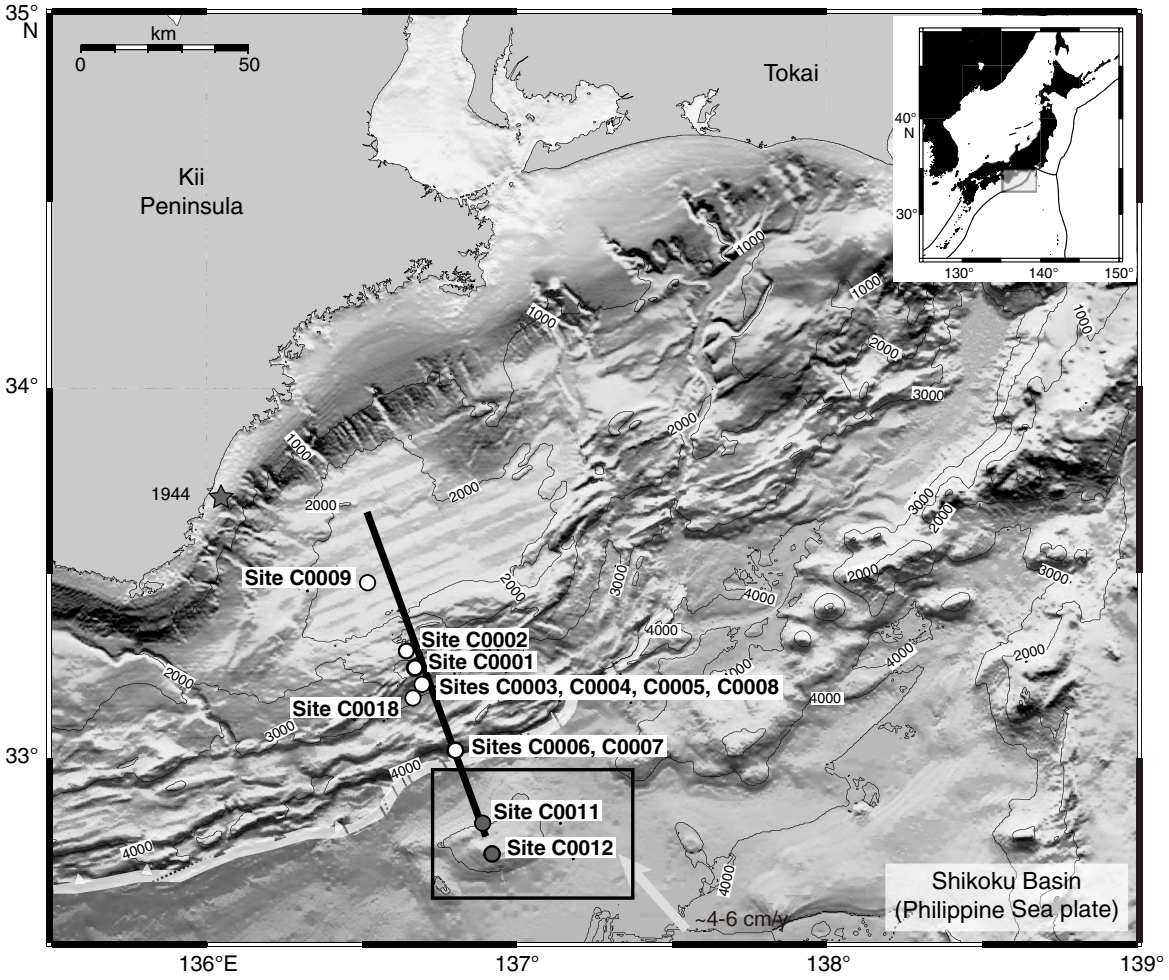

Figure F2. Location of NanTroSEIZE Sites C0011 and C0012 on a seismic profile of Nankai accretionary prism off Kii Peninsula.

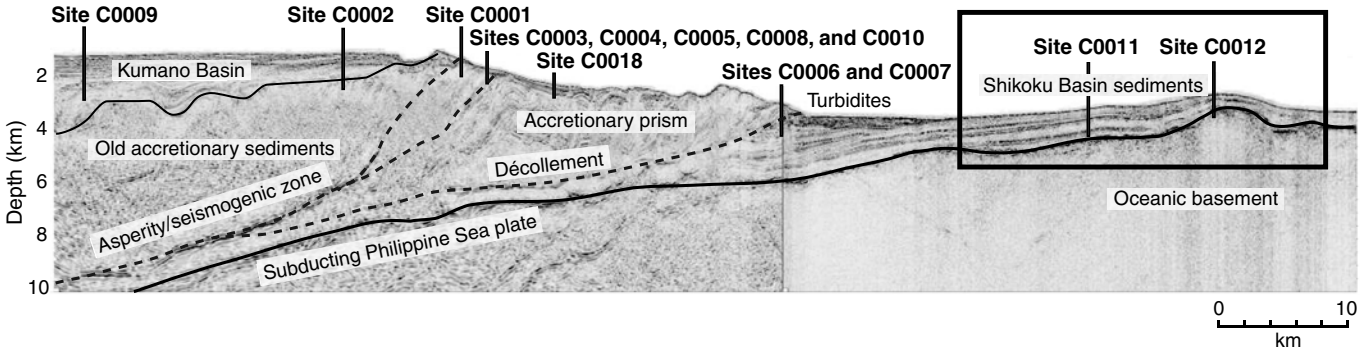

Figure F3. Stratigraphic summary, Site C0011. Open diamonds = locations and porosities of tested samples.

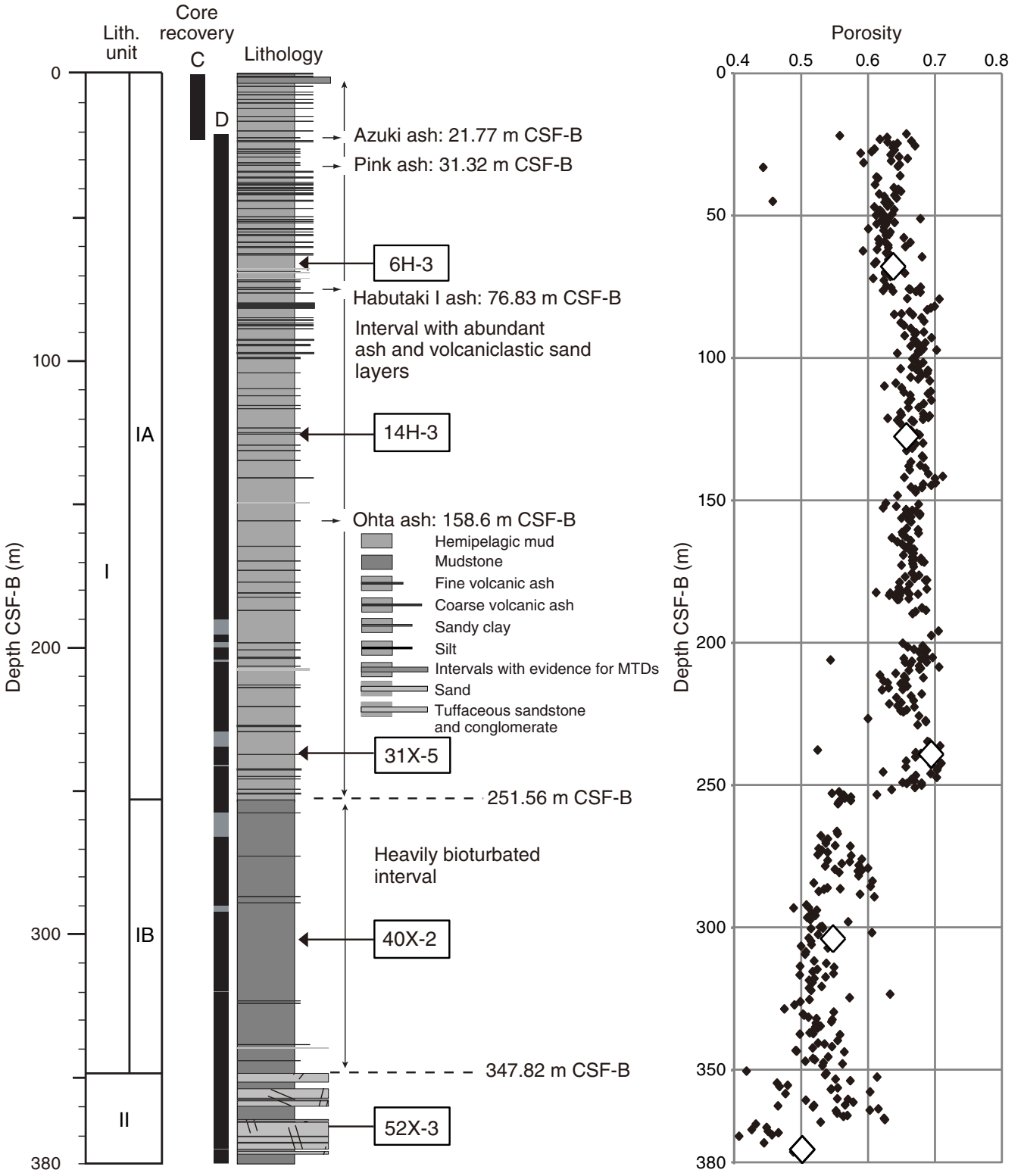

Figure F4. Stratigraphic summary, Site C0012. Open diamonds = locations and porosities of tested samples.

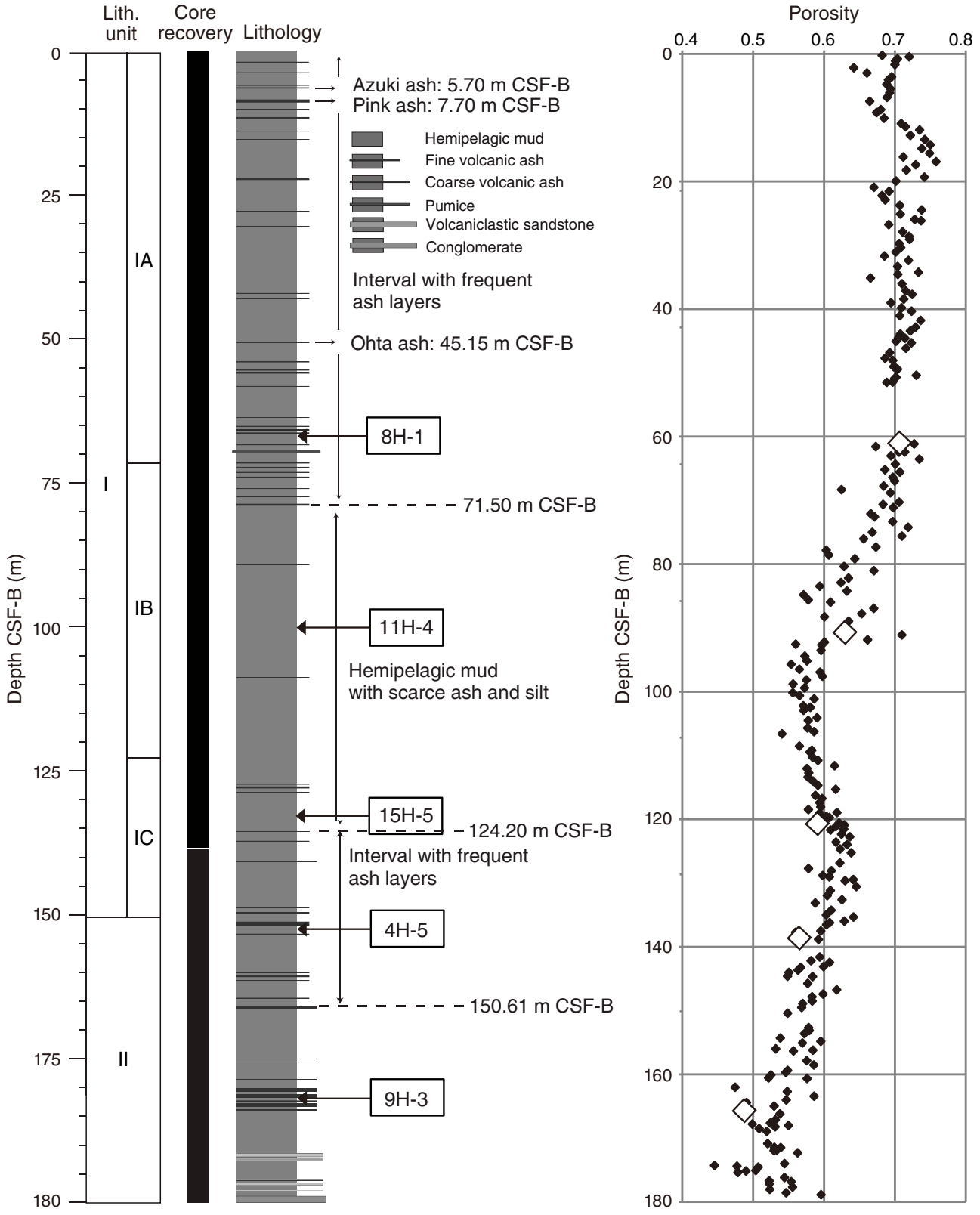

Figure F5. Schematic diagram of equipment for velocity measurements.

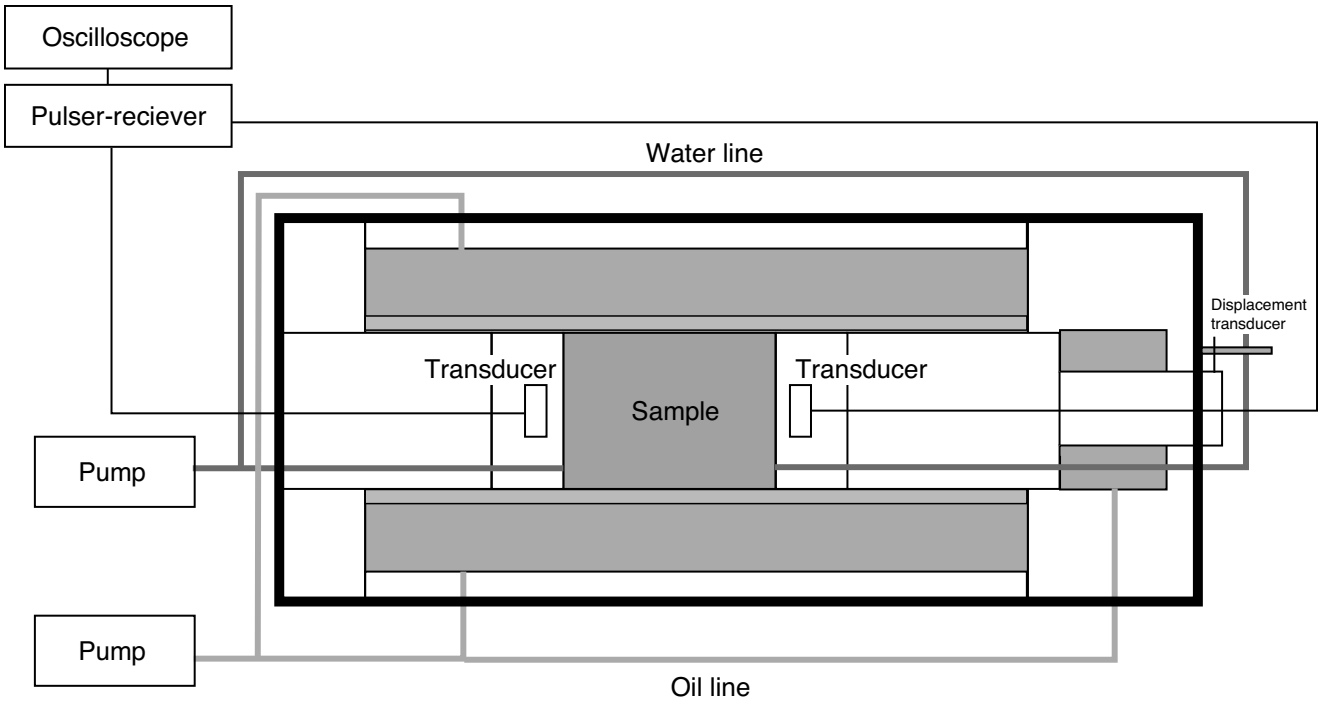

Figure F6. Compressional wave velocity vs. effective pressure, Sites C0011 and C0012. Gray diamonds = velocities under in situ effective pressure.

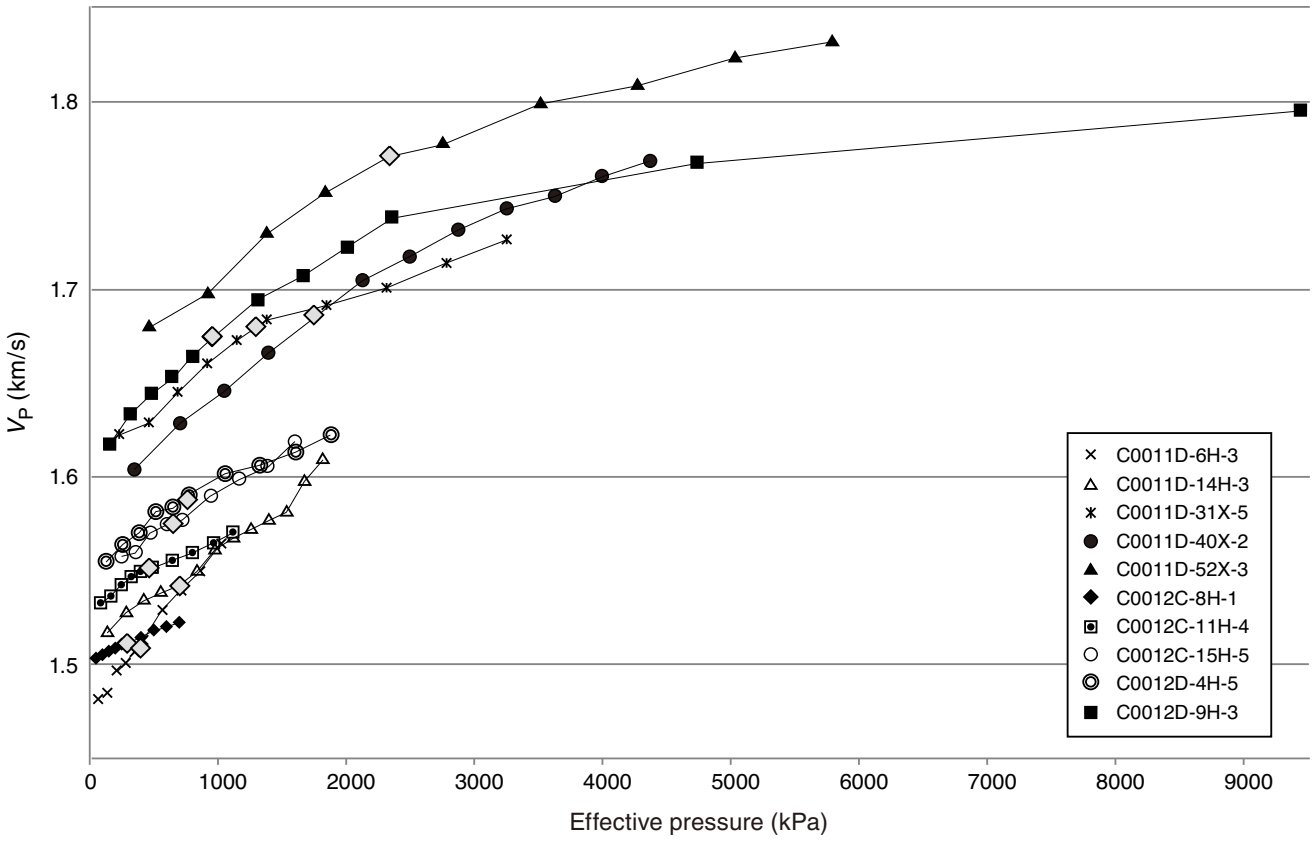

Figure F7. Porosity vs. effective pressure, Sites C0011 and C0012. Gray diamonds = porosities under in situ effective pressure.

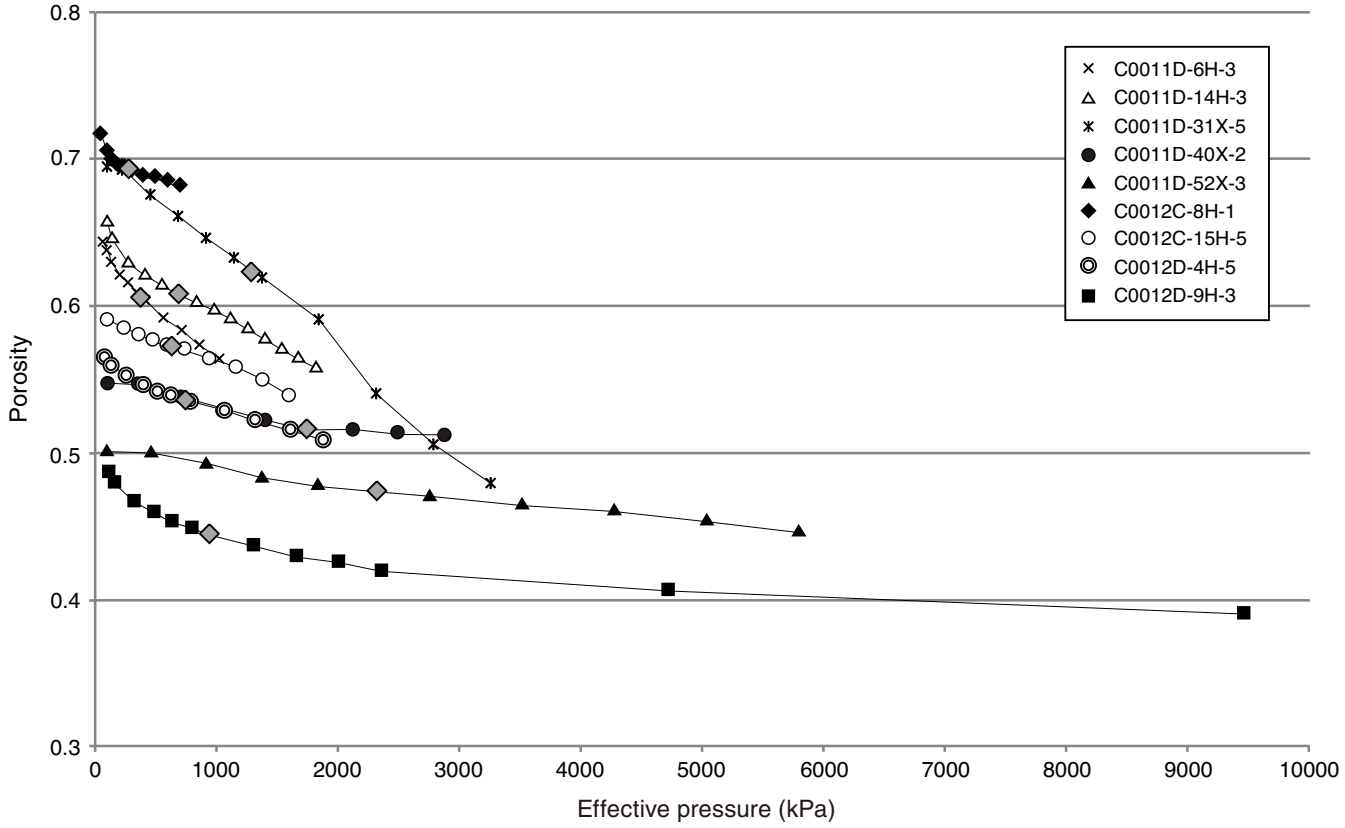

Figure F8. Compressional wave velocity vs. porosity, Sites C0011 and C0012. Gray diamonds = velocities and the porosities under in situ effective pressure. Gray dots = velocity (*z*-direction) and porosity from onboard measurements.

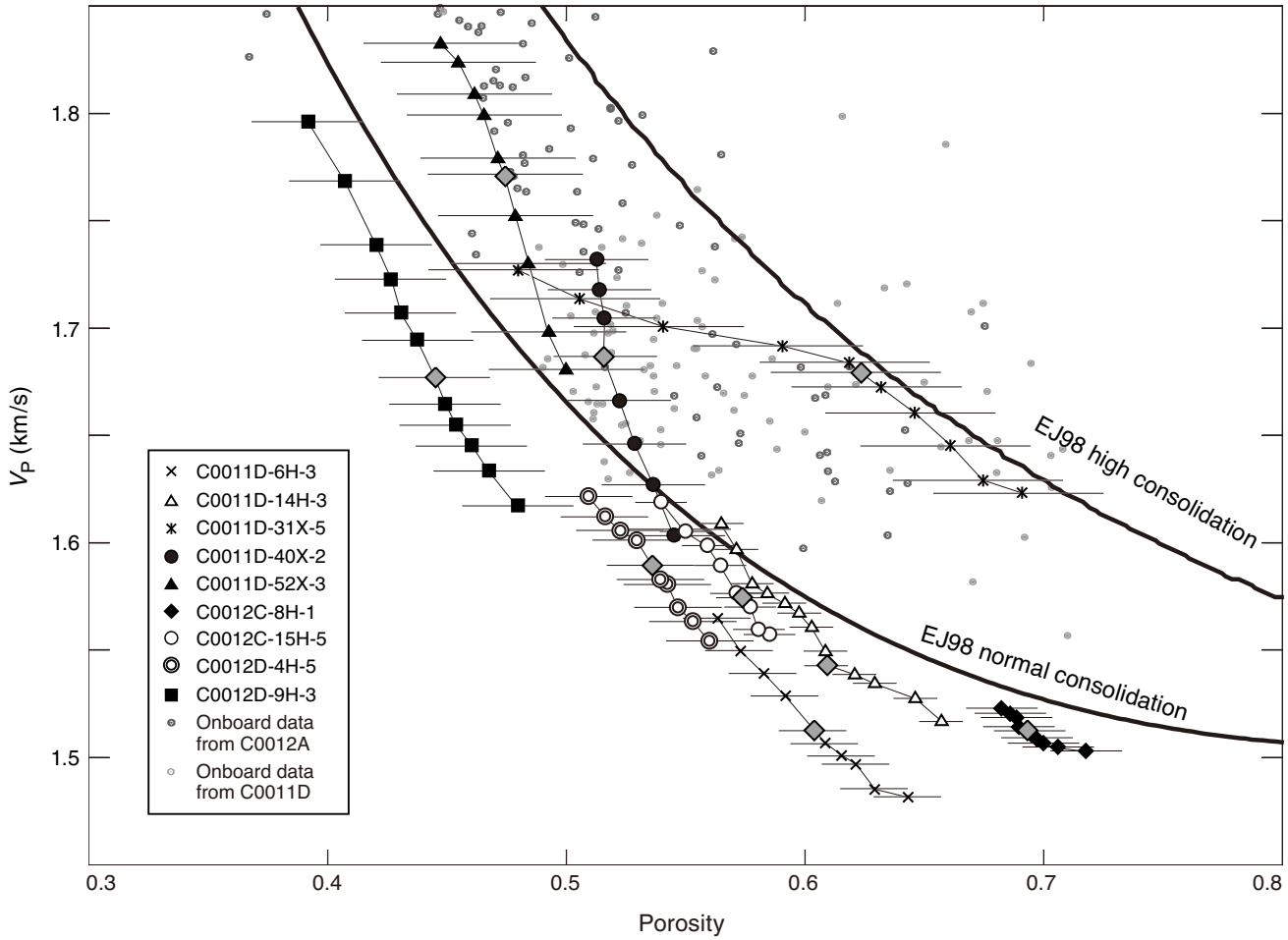

Figure F9. Compressional wave velocities from laboratory experiments under in situ effective pressure, onboard measurements (Holes C0011D and C0012A), and logging while drilling (LWD) (Hole C0012H).

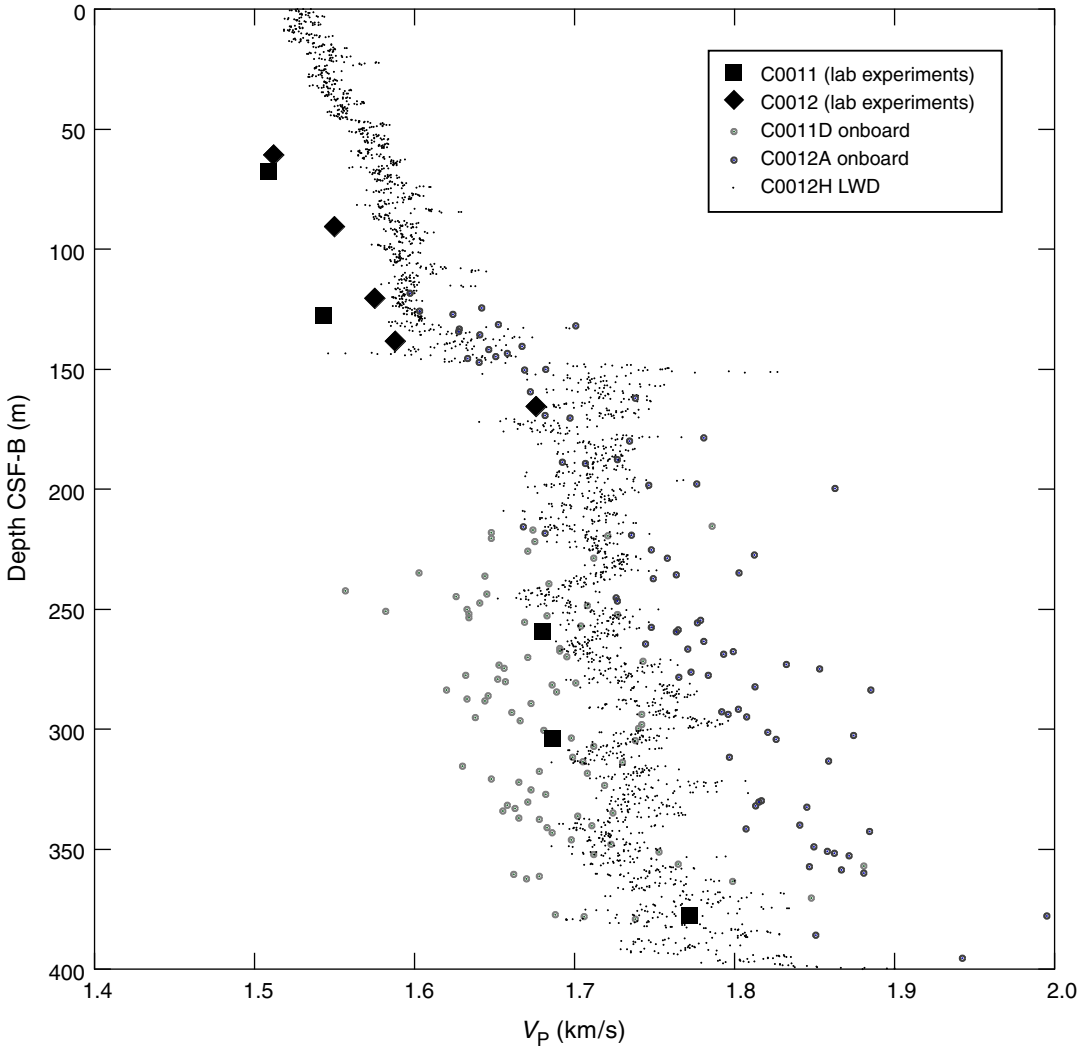

Table T1. Effective pressure, compressional wave velocity, and porosity for tested samples.

Hole, core, section	Depth CSF (m)	Effective pressure (kPa)	V_P (km/s)	Porosity
333-				
C0011D-6H-3	67.869	70	1.481	0.643
		140	1.485	0.630
		210	1.497	0.621
		280	1.501	0.616
		350	1.507	0.609
		383	1.509	0.606
		420	1.513	0.604
		570	1.529	0.592
		720	1.539	0.583
		870	1.550	0.574
		1020	1.564	0.564
C0011D-14H-3	127.582	140	1.517	0.646
		280	1.528	0.629
		420	1.534	0.621
		560	1.539	0.615
		693	1.543	0.609
		700	1.543	0.609
		840	1.550	0.603
		980	1.561	0.598
		1120	1.568	0.592
		1260	1.572	0.585
		1400	1.577	0.578
		1540	1.581	0.571
		1680	1.598	0.565
		1820	1.609	0.558
C0011D-31X-5	239.21	230	1.623	0.691
		460	1.629	0.675
		690	1.645	0.661
		920	1.660	0.646
		1150	1.672	0.632
		1296	1.680	0.624
		1380	1.684	0.619
		1850	1.692	0.591
		2320	1.701	0.541
		2790	1.714	0.506
		3260	1.727	0.480
C0011D-40X-2	304.01	350	1.603	0.545
		700	1.627	0.537
		1050	1.646	0.529
		1400	1.666	0.522
		1745	1.686	0.517
		1750	1.687	0.517
		2125	1.705	0.516
		2500	1.718	0.514
		2875	1.732	0.513
		3250	1.743	ND
		3625	1.750	ND
		4000	1.760	ND
		4375	1.768	ND
C0011D-52X-3	378.06	460	1.680	0.500
		920	1.698	0.493
		1380	1.730	0.484
		1840	1.752	0.479
		2300	1.772	0.475
		2326	1.772	0.474
		2760	1.779	0.471
		3520	1.799	0.466
		4280	1.809	0.462
		5040	1.823	0.455
		5800	1.832	0.447
C0012C-8H-1	60.902	50	1.503	0.718
		100	1.505	0.706
		150	1.507	0.700
		200	1.509	0.697
		250	1.511	0.695
		282	1.512	0.694
		300	1.513	0.693
		400	1.515	0.690
		500	1.519	0.689
		600	1.521	0.686
		700	1.523	0.683
C0012C-11H-4	90.76	80	1.532	ND
		160	1.536	ND
		240	1.543	ND
		320	1.547	ND
		400	1.549	ND
		442	1.550	ND
		480	1.551	ND
		640	1.556	ND
		800	1.560	ND
		960	1.564	ND
		1120	1.571	ND
C0012C-15H-5	120.55	120	ND	0.589
		240	1.558	0.585
		360	1.560	0.581
		480	1.570	0.577
		600	1.575	0.574
		641	1.575	0.573
		720	1.577	0.571
		940	1.590	0.565
		1160	1.599	0.559
		1380	1.606	0.550
		1600	1.619	0.540
C0012D-4H-5	138.561	130	1.555	0.560
		260	1.563	0.553
		390	1.570	0.547
		520	1.581	0.542
		650	1.583	0.540
		752	1.588	0.536
		780	1.590	0.536
		1055	1.601	0.530
		1330	1.606	0.523
		1605	1.613	0.516
		1880	1.622	0.509
C0012D-9H-3	165.734	160	1.617	0.480
		320	1.634	0.468
		480	1.645	0.460
		640	1.655	0.454
		800	1.665	0.449
		946	1.676	0.445
		960	1.677	0.445
		1310	1.694	0.438
		1660	1.707	0.431
		2010	1.723	0.427
		2360	1.739	0.421
		4730	1.768	0.407
		9460	1.796	0.392

Shaded cells = parameters at in situ conditions. ND = not determined.